

Article

Investigating the Impact of Spatiotemporal Variations in Water Surface Optical Properties on Satellite-Derived Bathymetry Estimates in the Eastern Mediterranean

Fickrie Muhammad ^{1,2,*} , Ioannis Tsimpouxis ^{1,3}  and Harald Sternberg ¹ 

¹ Department of Hydrography and Geodesy, HafenCity University Hamburg, 20457 Hamburg, Germany; i.tsimpouxis@gmail.com (I.T.); harald.sternberg@hcu-hamburg.de (H.S.)

² Hydrography Research Group, Faculty of Earth Sciences and Technology, Bandung Institute of Technology, Bandung 40132, Indonesia

³ Hellenic Navy, 15561 Athens, Greece

* Correspondence: fickrie.muhammad@hcu-hamburg.de; Tel.: +49-15217927164

Abstract: Bathymetric data are crucial for benthic monitoring in coastal areas but are traditionally obtained through costly and geographically limited acoustic methods. This study uses satellite-derived bathymetry (SDB) in the Eastern Mediterranean, focusing on the Cretan Sea in Greece. It explores how variations in water surface optical properties affect SDB models over four years (2019–2022), using Sentinel-2 satellite data. The research covers two areas with contrasting features: the Chania Gulf and the open waters around Chrissi Island. Three methodologies were tested: the band-ratio method, the linear-logarithmic method, and an inherent optical properties linear model. Significant spatiotemporal variations in the SDB models were found, due to seasonal changes in water surface properties, such as temperature and suspended organic materials. Linear optical properties-based methods performed best, achieving a mean RMSE close to 1 m, slightly outperforming the ratio-based method. The logarithmic method was less effective, with RMSE values ranging from 1.3 to 1.5 m. A preliminary Kalman filter (KF) analysis increased RMSE to the decimeter level. This study demonstrates the impact of water surface optical properties on SDB models. It highlights the value of SDB for cost-effective, high-resolution coastal mapping in complex coastlines like those in Greece.

Keywords: satellite-derived bathymetry (SDB); water optical properties; Mediterranean waters; empirical method; Kalman filter (KF)



Academic Editor: Biao Zhang

Received: 18 October 2024

Revised: 23 January 2025

Accepted: 24 January 2025

Published: 28 January 2025

Citation: Muhammad, F.; Tsimpouxis, I.; Sternberg, H. Investigating the Impact of Spatiotemporal Variations in Water Surface Optical Properties on Satellite-Derived Bathymetry Estimates in the Eastern Mediterranean. *Remote Sens.* **2025**, *17*, 444. <https://doi.org/10.3390/rs17030444>

Copyright: © 2025 by the authors. Licensee MDPI, Basel, Switzerland. This article is an open access article distributed under the terms and conditions of the Creative Commons Attribution (CC BY) license (<https://creativecommons.org/licenses/by/4.0/>).

1. Introduction

Seafloor topography, or bathymetry, is vital for various marine activities. Accurate bathymetric maps and data are crucial for navigational safety, helping surface ships, submarines, and remote vehicles to avoid underwater hazards and chart safe, efficient routes. Traditionally, bathymetric data have been gathered using shipborne systems with echo sounders and airborne systems with LiDAR. While these methods are precise, they are also expensive, labor-intensive, and geographically limited, restricting the frequency of surveys. As a complementary approach, satellite-derived bathymetry (SDB) offers additional data in a fast and cost-efficient way, particularly for shallow waters (less than 30 m deep), by deriving seabed depths from high- to medium-resolution multispectral satellite imagery. SDB enhances them by enabling the mapping of remote and hard-to-reach areas, filling critical gaps in global bathymetric data at the same time [1].

Advancements in remote sensing technologies have expanded bathymetric research, mainly through high-resolution satellite imagery [2]. Multispectral sensors, especially the green and blue bands, can penetrate up to 25 m below the sea surface in clear water [3]. Sentinel-2 MSI sensors, with 10-m spatial resolution, support bathymetric tasks using freely available datasets. Seafloor topography is dynamic, influenced by natural phenomena like tides, storms, sediment deposition, and human activities such as dredging, fishing, and underwater construction. These changes can be spatial and temporal, making studying spatiotemporal variations in SDB estimates crucial.

The foundational methodology was established in the 1970s [4] and is employed in high-transparency waters with a homogeneous bottom. The method differentiates the radiances between pixels due to depth differences. Each radiation wavelength penetrates to different depths within the water column and decays exponentially, with the bottom albedo assumed to be constant [5]. In Ref. [3], the satellite spectral bands are considered to have different attenuation rates, requiring minimal calibration data. The authors of Ref. [6] analyzed optical water properties, sourcing detailed information on the water column's optical properties. Tests in waters with a uniform, sand-type bottom showed that the method works for any radiation wavelength and water category. Furthermore, the inherent optical properties derived from satellite imagery are used in Ref. [7] to estimate SDB, enabling direct analysis without additional sampling.

This study focuses on the Eastern Mediterranean, specifically Chrissi Island and the Chania Gulf, examining optical properties like absorption, backscattering, and diffuse attenuation coefficients. Greece's aquatic environment presents both challenges and opportunities for remote-sensing bathymetry, with stable year-round conditions and clear waters conducive to SDB, which has the potential to revolutionize hydrographic surveying. SDB's cost-effectiveness and high-resolution capabilities make it ideal for addressing maritime landscape challenges, from defense and marine trade to scientific research and environmental conservation [8,9].

The Eastern Mediterranean's unique geological and environmental characteristics further complicate these issues. Factors such as seasonal weather patterns, water characteristics, and human activities can impact the reliability and applicability of SDB estimates. Therefore, a focused study was conducted on the spatiotemporal variations in SDB in this region. This study aimed to understand how variations in water surface optical properties affect SDB estimates over time and space. The research addressed several sub-questions, including the impact of seasonal and weather patterns, integrating different satellite-derived products, and choosing satellite image quality and atmospheric correction processors. To achieve these objectives, this study followed a structured approach. This began with downloading seasonal satellite imagery and merging the best images over five years. The data underwent rigorous preprocessing to ensure high quality, including atmospheric, sunglint, and water surface corrections. Bathymetric information was then extracted and compared with ground truth data for validation.

The study extended beyond bathymetric mapping to evaluate water surface properties, specifically its inherent optical properties (IOPs) and apparent optical properties (AOPs) across seasons. This evaluation helped to understand their influence on SDB estimates and their relevance to hydrographic surveying. Comparative analysis between bathymetry and seasonal variations in IOPs and AOPs provided valuable insights. For future research, data assimilation aimed to refine depth estimations with in situ measurements. However, additional steps, such as error modeling and algorithm adjustments, are needed.

2. Materials

2.1. Study Area

The study area focuses on Crete Island, located in Greece, which lies in the southern Aegean Sea, part of the Eastern Mediterranean basin. The island extends approximately between the meridians $23^{\circ}28'E$ and $26^{\circ}21'E$ and between the parallels $34^{\circ}46'N$ and $35^{\circ}40'N$. The broader study area is situated on Crete, surrounded by the deepest basin in Greece, with a depth of approximately 2500 m in the southern Aegean region. This basin interacts with the Levantine Basin and the Ionian Sea through the eastern and western straits of Crete Island [10].

For SDB estimation, the area is classified into two distinct areas of interest (AOI), as seen in Figure 1. The first study area is an embayment of the Cretan Sea, located northwest of Crete Island, and is called the Chania Gulf, named after the local city. It has a length of approximately 22 km, a mean latitude of $35^{\circ}33'N$, and a mean longitude of $23^{\circ}54'E$. The second study area is located on Chrissi Island, in the southeastern (SE) part of Crete, approximately 15 km offshore from Ierapetra city, with a mean latitude of $34^{\circ}52'N$ and a mean longitude of $25^{\circ}42'E$.

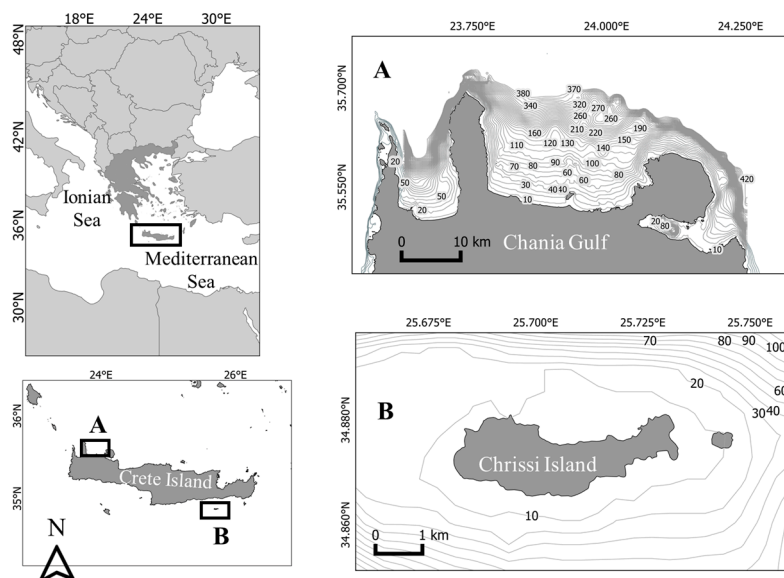


Figure 1. The study area is situated in the Cretan Sea and is divided into two AOI: (A) the Chania Gulf, and (B) Chrissi Island. The SDB in both areas is focused on the shallow water in the shallow coastal waters, as indicated by the contour line (in meters) with a maximum depth of 30 m.

Generally, the waters are transparent, and the seabed is dominated by sandy substrates with a few rocky outcrops [11]. The western part is included in the NATURA2000 network, with the code GR4340003 [12]. In contrast, the marine part is delimited by a depth curve of 50 m and is characterized by the presence of *Posidonia oceanica* meadows. However, it should be noted that the bathymetry increases significantly in the area. Hence, only coastal areas up to 30 m depth are optimal for generating SDB estimates [12]. The tidal signal is also 15 cm and can be neglected for SDB estimates [8]. The anthropogenic activity is more dominant than Chrissi Island because Chania is a well-known tourist destination, with fishing areas and sea sports activities conducted from late spring to late autumn.

A typical Mediterranean climate with mild, rainy winters and hot, dry summers characterizes Crete Island. The atmosphere can be quite humid, depending on the proximity to the sea, while winter is relatively mild [11]. The complex ocean circulation patterns and water mass interactions can result in localized areas of higher nutrient concentrations, especially in upwelling zones or regions with vigorous vertical mixing [10]. The study

areas were selected firstly because of the profound water clarity and secondly because of the different properties of the AOI. The Chania Gulf is a more enclosed area of Crete Island, while Chrissi Island is in open seas. Hence, investigating SDB estimates under different hydrodynamic conditions can yield significant insights for the Eastern Mediterranean.

2.2. Satellite Data

Sentinel mission products are freely available for download via the Copernicus Open Access Hub. This study used Level-1C raw satellite imagery to extract the water's optical properties, utilizing adjustable atmospheric correction parameters. As indicated in Table 1, the imagery for the Chania Gulf and Chrissi Island, spanning from 2019 to 2022, was filtered by month and limited to images with 2% or less cloud coverage. The selected period aligns with recent in situ measurements and was extended by five years to capture significant bathymetry changes. Sun-zenith angle (SZA) products above 70° were also excluded to reduce solar reflection [13]. Additionally, the glint angle was calculated using the view zenith angle, view azimuth angle, sun azimuth angle, and sun zenith angle, based on the principles of radiative transfer theory (RTE) [14]. A smaller glint angle indicates more direct sunglint being reflected in the imagery.

Table 1. Sentinel-2 level 1 C data, curated for SDB modeling.

Year	Season	Sensing Date (UTC Time)	Sun Zenith Angle (Degree)	Sun Azimuth Angle (Degree)	View Zenith Angle (Degree)	View Azimuth Angle (Degree)	Glint (Degree)
Chania Gulf							
2019	Spring	07-March-2019	44.59	152.74	3.05	215.23	43.25
	Summer	09-August-2019	25.11	137.32	3.09	215.46	24.65
	Autumn	28-October-2019	49.99	164.69	3.13	213.80	47.98
2020	Winter	31-January-2020	56.19	157.58	3.11	213.76	54.50
	Summer	28-August-2020	30.05	146.45	3.16	216.21	29.09
	Autumn	07-September-2020	33.02	150.82	3.16	216.19	31.82
2021	Spring	06-March-2021	44.77	152.84	3.16	216.12	43.42
	Summer	24-June-2021	18.9	125.73	3.12	214.59	19.08
	Autumn	07-October-2021	43.03	160.88	3.15	215.14	41.25
2022	Winter	19-February-2022	50.32	154.85	3.14	214.94	48.81
	Summer	18-August-2022	27.26	141.65	3.18	216.57	26.59
	Autumn	27-October-2022	49.76	164.60	3.14	214.76	47.79
Chrissi Island							
2019	Spring	19-March-2019	39.50	149.45	3.56	122.09	36.37
	Summer	21-August-2019	27.70	140.30	3.51	123.17	24.37
	Autumn	25-October-2019	48.36	163.00	3.51	123.16	45.71
2020	Winter	23-January-2020	57.44	157.70	3.56	122.27	54.56
	Summer	30-August-2020	30.28	145.03	3.51	123.42	27.04
	Autumn	13-November-2020	54.27	164.79	3.47	123.74	51.69
2021	Spring	13-March-2021	41.63	150.29	3.50	123.10	38.54
	Summer	30-August-2021	30.21	144.91	3.49	122.66	27.01
	Autumn	24-October-2021	48.20	162.93	3.45	125.80	45.49
2022	Winter	11-February-2022	52.44	154.67	3.50	123.60	49.47
	Summer	20-August-2022	27.53	139.93	3.57	122.69	24.14
	Autumn	04-October-2022	41.31	158.50	3.50	123.49	28.49

2.3. Field Data

In the empirical SDB estimations used in this study, field data were used to calibrate and validate the SDB models. For Chrissi Island, ground truth data came from the Hellenic Navy Hydrographic Service's Electronic Navigational Chart (ENC) GR3CFDES (scale 1:90,000), last updated on 23 February 2022, with depths referenced to the low astronomical tide (LAT). For the Chania Gulf, the Hellenic Center for Marine Research collected data during bathymetric surveys from January 2014 to May 2015. Instruments included a

Humminbird single-beam echo sounder (SBES) and a Reson 7125 dual-head multibeam echo sounder (MBES). Positioning errors were reduced using a real-time kinematic (RTK) solution from the Hellenic Positioning System (HEPOS), with depth corrections applied for LAT and the sensor's draught [11]. Calibration data consisted of approximately 20 to 25 points distributed in depths from 2.4 m up to 24 m for both study areas, as shown in Figure 2.

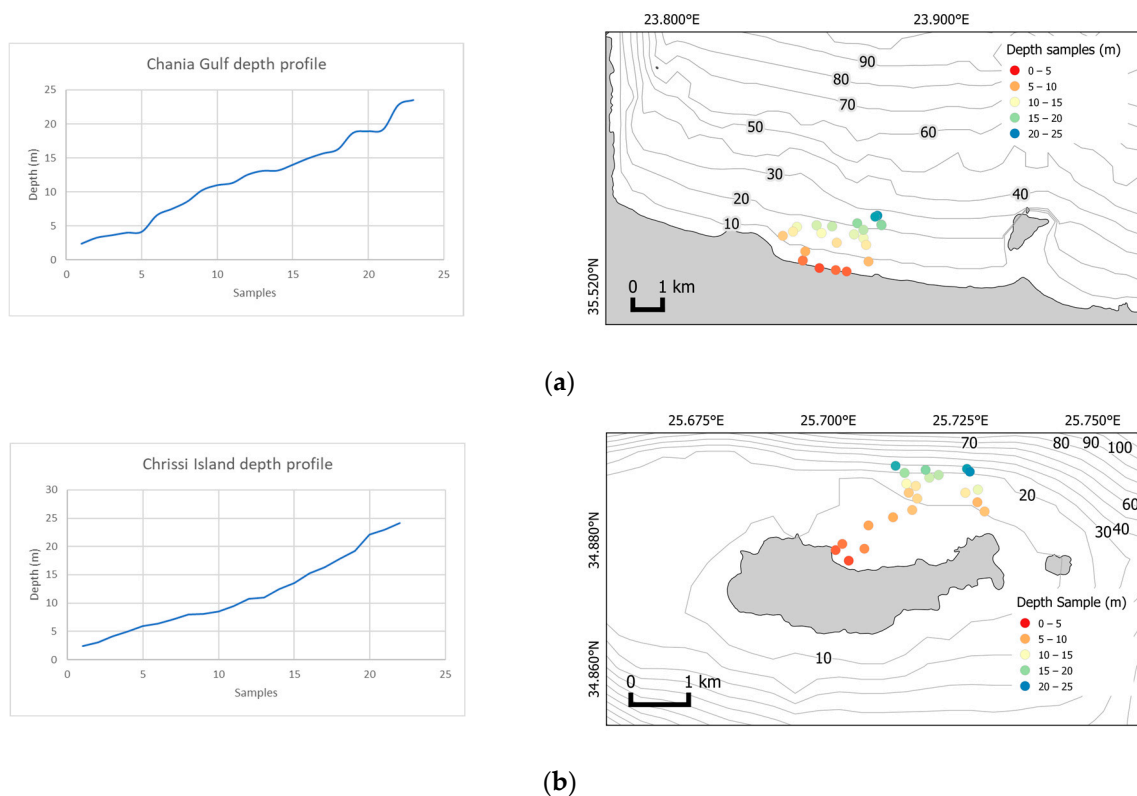


Figure 2. The calibration data for both AOIs are presented, illustrating the depth profiles in the figures on the right and the spatial distribution, with contour units expressed in meters: (a) Chania Gulf, where the samples were derived from the island's northern part, where the slope is smoother compared to the southern part; (b) Chrissi Island, where depth samples were considered in the middle of the Gulf as the best representation of the area's geomorphology.

3. Methods

3.1. Empirical Satellite-Derived Bathymetry (SDB)

In the current study, the SDB models under investigation are the linear-logarithmic algorithm proposed in Ref. [4], the band-ratio transformation developed by the authors of Ref. [3], and the inherent optical properties linear model (IOPLM) proposed in Ref. [7]. Lyzenga developed a method for studying marine environments with low suspended particle, chlorophyll, and organic matter levels. This method assumes that the physical and chemical properties of the water surface depicted in a satellite image remain consistent. The ratio of attenuation coefficients due to light diffusion in two spectral zones should remain constant across the entire image [15]. However, this assumption may only hold in some cases, as reflectance from the water bottom may vary depending on the sediment composition.

For satellite observations, the total radiance signal (L_t) is a sum of atmospheric path radiance (L_p), specular radiance (L_s), subsurface volumetric radiance (L_v), and the bottom radiance (L_b), with both L_b and L_v contributing to water-leaving radiance (L_w) in the deep water [9,16,17]. Proper atmospheric correction to minimize the atmospheric radiance and

sunglint removal to minimize the specular radiance is critical, as ignoring it can lead to significant errors in depth estimation [18]. The water-leaving reflectance (R) itself is derived from the relationship between water-leaving radiance (L_w) and downwelling radiance (E_d) [19], as expressed by the following equation:

$$R = \frac{L_w}{E_d} \quad (1)$$

One spectral band's use for deriving depth estimates is primarily based on the reflectivity of the seabed, also known as albedo. If the reflectivity of the seafloor decreases, it can lead to an overestimation of sea depth. However, shortly after its first use, it was discovered that analyzing two spectral bands can account for the variability of the seafloor's reflectivity [15]. This results in a more precise estimation of depth, which can be calculated using the following equation:

$$z = \alpha_0 + \alpha_i \cdot \ln[R_{rs}(\lambda_i) - R_\infty(\lambda_i)] + \alpha_j \cdot \ln[R_{rs}(\lambda_j) - R_\infty(\lambda_j)] \quad (2)$$

where R_{rs} is the atmospherically corrected value of the water-leaving reflectance R , accumulated as remote sensing radiance for band λ_i , R_∞ is the reflectance of the optically deep water areas of the image, α_0 , α_i , and α_j are the multiple regression analysis coefficients, and z is the estimated water depth.

A significant disadvantage of the linear-logarithmic algorithm in coastal environments consisting of underwater vegetation, such as algae or seagrass, is that the bottom reflectance in shallow water is lower than that in deep water $R_\infty(\lambda_i)$. As a result, in shallower waters, the difference $[R_{rs}(\lambda_j) - R_\infty(\lambda_j)]$ is smaller than zero; thus, the natural logarithm $\ln[R_{rs}(\lambda_j) - R_\infty(\lambda_j)]$ is not defined. The different spectral zones of passive sensors exhibit distinct spectral absorptions (attenuations), and the depth values in the Lyzenga equation vary as a function of the logarithm; therefore, the ratio of the logarithms, for example, between blue and green bands, will also change according to the depth.

A variation in the bottom albedo, caused by changes in underwater vegetation or sediment, affects both spectral zones similarly, while changes in depth significantly impact the zone with higher absorption. Thus, the variation in the reflectance ratio between spectral zones due to depth will be much more significant than the variation caused by changes in bottom quality [20]. Consequently, when investigating a coastal area with a constant depth but different bottom compositions, satellite imagery pixels displaying varying reflectance due to sediment and vegetation will have a nearly consistent logarithmic reflectance ratio. A ratio transform algorithm to determine the bottom depth has been proposed in Ref. [3], regardless of the bottom quality or the existing vegetation. It can be calibrated to actual depths using data from a nautical chart or a bathymetric plot or through field measurements, using the following mathematical formula:

$$z = m_1 \cdot \frac{\ln(n \cdot R_{rs}(\lambda_i))}{\ln(n \cdot R_{rs}(\lambda_j))} - m_0 \quad (3)$$

where m_1 is an adjustable constant, which serves to tune the ratio to the depth of the chart or field measurements, n is a constant that is associated with the area of interest, and m_0 is an offset constant for the depth that corresponds to 0 m ($z = 0$). It should be noted that the constant n is chosen to ensure that the logarithm is always positive, so the ratio produces linear or proportional results as a function of the change in depth. In addition, the coefficients m_1 and m_0 can be determined by statistically correlating the reflectance values and field data at the corresponding pixel positions.

The final SDB method tested in this study is based on the IOPs and their fluctuations with depth, using a model found in the IOPLM that was developed by the authors of Ref. [7]. This model utilizes the blue and green bands from WorldView-2 multispectral images, which offer very high resolution, to gather a wide range of water depth data. The formula consists of the following components:

$$z = \alpha \cdot \frac{u(\lambda_i)}{u(\lambda_j)} + b \quad (4)$$

where α and b are the regression coefficients, and $u(\lambda_i)$ and $u(\lambda_j)$ are the inherent optical parameters of the blue band (i) and the green band (j), related to the absorption and backscattering coefficient. Lastly, z is the depth estimation.

Finally, the inherent optical property parameter u can be calculated from the following equation:

$$u(\lambda) = \frac{-p_0 + \sqrt{(p_0)^2 + 4 \cdot p_1 \cdot r_{rs}(\lambda)}}{2 \cdot p_1} \quad (5)$$

Here, p_0 and p_1 are model constants that change with various optical water properties. Their values may vary with the particle phase function and differ from ocean to coastal waters. For application to both coastal and open water bodies, the authors of Ref. [6] used the averaged values $p_0 = 0.0895$ and $p_1 = 0.1247$ to develop the multiband quasi-analytical algorithm (QAA). This algorithm aimed to retrieve the absorption and backscattering coefficients from the remote-sensing reflectance of optically deep waters. Because u is just a ratio of the backscattering coefficient to the sum of absorption and backscattering coefficients, knowledge of the absorption coefficient enables estimating the backscattering coefficient and vice versa.

In addition, $r_{rs}(\lambda)$ is the subsurface remote sensing reflectance. It can be obtained by the conversion of the atmospherically corrected reflectance $R_{rs}(\lambda)$ [21], as follows:

$$r_{rs}(\lambda) = \frac{R_{rs}(\lambda)}{(0.52 + 1.7 \cdot R_{rs}(\lambda))} \quad (6)$$

To summarize the steps of the last method, one has to start by calculating the subsurface reflectance $r_{rs}(\lambda)$ from the atmospherically corrected remote-sensing reflectance $R_{rs}(\lambda)$ for both the green and blue bands. In this case, R_{rs} is treated as equivalent to R_w , where the remote-sensing reflectance includes contribution from water, atmosphere, and glint. Then, we derive the inherent optical parameter u from Equation (6) for both blue and green bands. Finally, the ratio of the u parameter between the two bands is plotted (scatter plot) against the field measurements, and, after regression analysis, the regression coefficients are deduced. This linear equation is the SDB estimation for the scene of interest.

In addition, the SDB estimations following the atmospheric correction (AC) were also subjected to this process. Initially, the Acolite, developed by the Royal Belgian Institute (RBINS) using a dark spectrum fitting (DSF) [22,23] processor, was used as the main AC because of its superiority, as highlighted in Ref. [24]. The tool automatically calculates the water's optical parameters using the QAA method, by which the linear band response to the field data can be analyzed. However, the SDB estimations for the summer period utilized the Case 2 Regional CoastColour (C2RCC) algorithm [25]. The C2RCC showed better handling in areas where sunglint was found in the images, while the Acolite DSF returning zero values led to failure in estimating the SDB. Conversely, an important note is that this IOPLM method was initially developed for very high spatial resolution (~ 2 m) satellites such as WV-2, SPOT, and Pleiades. In this study, the Sentinel-2 products belong to

the high spatial resolution group, and all the tests were executed with a best value of 10 m of visible bands.

In conclusion, two factors primarily influenced the selection of the three methodologies mentioned above for remote-sensing bathymetric derivation. Firstly, these methodologies are based on distinct principles and utilize different techniques for depth estimation, thereby providing a diverse and comprehensive approach. Secondly, they offer varying approaches to the relationship with the water's optical properties, a crucial aspect of this research. Within this context, the linear transformation technique does not accommodate variations in the water's optical properties, operating under the assumption of a state of homogeneous water properties throughout the testing period. Conversely, the other two methodologies integrate the variability of the water's optical properties into their computation, providing a more dynamic representation of the aquatic environment.

The technique of band ratio transformation accommodates the oscillations in the water's optical properties indirectly by measuring the actual responses of the spectral bands, which encapsulate the influence of these optical properties. Conversely, the IOPLM method operates on a more direct principle. It is grounded on the inherent optical parameter 'u', which explicitly incorporates the responses associated with absorption and scattering phenomena within the water surface.

3.2. Kalman Filter (KF) Smoothing

The Kalman filter is an algorithm used to estimate the state of a linear dynamic system in the presence of uncertainty and noise. It operates through two main steps: prediction and update. In the prediction step, the filter estimates the system's next state, based on the current state and control inputs [26]. The filter utilized in this study uses the SDB estimates as the initial state. In contrast, the field data is used as the measurement input for updating the bathymetry model, as shown in Equations (7)–(11).

$$X_{k|k-1} = F_k X_{k-1|k-1} + B_k c_k \quad (7)$$

$$P_{k|k-1} = F_k P_{k-1|k-1} F_k^T + Q_k \quad (8)$$

$$K_k = P_{k|k-1} H_k^T \left(H_k P_{k|k-1} H_k^T + R_k \right)^{-1} \quad (9)$$

$$X_{k|k} = X_{k-1|k-1} + K_k \left(z_k - H_k X_{k|k-1} \right) \quad (10)$$

$$P_{k|k} = \left(I - K_k H_k \right) P_{k|k-1} \quad (11)$$

The filtering involves calculating the predicted state estimate $X_{k|k-1}$ using the state transition model F_k with the control input model matrix B_k and any control inputs as vector c_k . While factors such as tides, currents, waves, and water properties can be used as control inputs in bathymetry, this study assumes these values to be negligible. Consequently, the identity matrix is defined for B_k . The state vector X_k here represents only the vertical information (depth), omitting the spatial and temporal dependencies. The index k denotes the predicted state, while $k - 1$ corresponds to the initial state, where the SDB estimate is treated as the initial state. It also includes the prediction of the estimate's uncertainty $P_{k|k-1}$ by considering both the previous uncertainty and the process noise Q_k .

The update step refines this prediction by incorporating new measurements, stored as measurement vector z_k . The Kalman gain K_k is calculated to determine how much the new measurement should influence the updated state estimate, with H_k as the observation model matrix relating the state vector to the measurement vector. The updated state estimate $X_{k|k}$ is then corrected using the Kalman gain, which adjusts the correction magnitude based on the difference between the predicted and actual measurements, also known as the

innovation or measurement residual. Finally, the estimated covariance $P_{k|k}$ is updated to reflect the reduced uncertainty after incorporating the measurement.

Through these iterative prediction and update steps, the Kalman filter continuously refines the state estimate, providing a more accurate and reliable estimate of the system's state over the number of sample SDB estimates, even in noise and uncertainty. The KF can be further refined and optimized based on the specific characteristics of the data, the research objectives, and the use of an iterative KF to model the error and reformulate the SDB equations.

3.3. Water's Optical Properties

The ocean's color is influenced by its optical properties, which are categorized into inherent optical properties (IOPs) and apparent optical properties (AOPs) [27]. IOPs depend only on the medium (seawater) and are not affected by external factors. Key IOPs include absorption, where light energy is converted to heat or chemical energy, and scattering, where light changes direction or wavelength [14]. AOPs are influenced by both the IOPs and the geometry of light propagation. AOPs include reflectance and diffuse attenuation coefficients, which describe how light is scattered or absorbed through water [28].

IOPs and AOPs are connected through the radiative transfer theory [14], where IOPs are used to calculate radiance, from which AOPs are derived. In remote sensing, inversion techniques are employed to estimate water surface properties like bio-optical parameters and seafloor depth from known radiance values [14,29]. Beyond the inversion techniques mentioned above, alternative, more empirical methods exist to assess the radiation propagation state within a specific water surface and remove the additive haze effect sourced from scattering. One such method is dark object subtraction (DOS), initially proposed by the authors of Ref. [30]. This technique is employed under the assumption that in deep-water regions, any radiation reflected from the seabed is virtually absent, due to high absorption levels. Consequently, the sensor's reflectance recordings in these regions are attributed solely to sources other than the bottom substrate. By subtracting the deep-water pixel values from the pixel values across the entire image set, it is posited that what remains is essentially the bottom reflectance.

In conclusion, the water surface's inherent and apparent optical properties are pivotal in determining the precision and dependability of satellite-derived bathymetry. These optical characteristics present both obstacles and avenues for methodological enhancements. Although factors such as water clarity, absorption, and scattering coefficients may impose constraints, this advancement in understanding their impacts and integrating corrective measures has contributed to the ongoing refinement of accurate and robust SDB algorithms.

3.4. Workflow

Despite the multitude of satellite-derived bathymetry models available for bathymetry estimate extraction, preprocessing is nearly ubiquitous across all techniques. The preliminary steps for SDB analysis include atmospheric correction for Level-1C products, image resampling, clipping the imagery to correspond with the study region, and the application of a sea-land mask using the NIR band (B8) of Sentinel-2A to spot marine features. After these preprocessing stages, the comprehensive methodology implemented in this study is conducted, as presented in the workflow chart in Figure 3.

and C2X-COMPLEX-Nets, intended primarily for inland waters. In this study, C2RCC-Nets were chosen because they best matched the conditions of the study area.

This study applied the logarithmic-linear band model [4], band-ratio transformation [3], and the IOP model [7] to analyze band responses to light attenuation. Acolite and C2RCC used non-linear least-squares calculations to compute key IOPs such as absorption and backscattering coefficients, turbidity, and suspended particulate matter (SPM) concentrations [35,36]. In addition, chlorophyll-a (Chl-a) concentrations were calculated using both processors' blue/green ratio algorithms. These Chl-a estimates provide insights into biological activity and seasonal variations in water properties, influenced by river runoff, water mixing, salinity, and temperature [34].

The preliminary Kalman filter (KF) implementation is also employed to mitigate the depth-related uncertainties derived by the SDB. The KF explicitly models depth-dependent uncertainties by accounting for increasing state estimation, measurement, and state transition noise with depth. With the Kalman gain set to depend more on the measurement than the update state, this approach shifts its reliance from noisy measurements to dynamically updated model estimates at greater depths, improving the accuracy and reliability of the bathymetric results.

To evaluate the accuracy of the SDB estimates, several error metrics were used. The root mean square error (RMSE) measures prediction accuracy, with lower values indicating closer alignment between satellite-derived depths and field measurements [37]. The mean absolute error (MAE) quantifies the average magnitude of errors without regard to direction, while the median absolute error (MedAE) provides a more robust measure against outliers [38]. The mean absolute percentage error (MAPE) expresses errors as a percentage, which is useful for comparing performance across different datasets [39]. These discrepancies in the in-depth estimates were compared to the S-44 Ed. 6 standard predictions for the total vertical uncertainty (TVU) associated with a Special Order survey [40]. Lower values across these metrics suggest more accurate depth estimations, indicating the effectiveness of this study's applied atmospheric correction and SDB methods.

4. Results

4.1. Atmospheric Correction

The Acolite DSF atmospheric processor demonstrated superior consistency, as highlighted by Caballero and Stumpf (2020), with repeatability and accuracy in scene-by-scene analyses, making it the primary AC algorithm used for all imagery. In contrast, the C2RCC processor showed lower accuracy and higher noise. However, C2RCC proved effective in retrieving depth information from scenes with moderate to severe sunglint, which is typical of summer imagery, underscoring its utility in challenging conditions. Figure 4 illustrates the visual results of atmospheric corrections on winter and summer 2022 imagery using the Acolite DSF and C2RCC models across both study areas.

It was found that the sunglint affected the performance of the Acolite DSF processor during the processing of summer imagery. Despite the inclusion of sunglint correction in the Acolite DSF, the output often resulted in black pixels, returning zero radiance value in the summer period. This obscured much of the area of interest, resulting in an inability to derive the SDB estimates using Acolite DSF. Caballero and Stumpf (2020) also reported this degradation when evaluating AC processors. Given its superior handling of sunglint, the C2RCC algorithm was chosen for summer scenes, producing minimal visible glint effects. In other seasons, however, the Acolite DSF processor was more robust, achieving an RMSE that was approximately 50 cm more accurate than C2RCC.

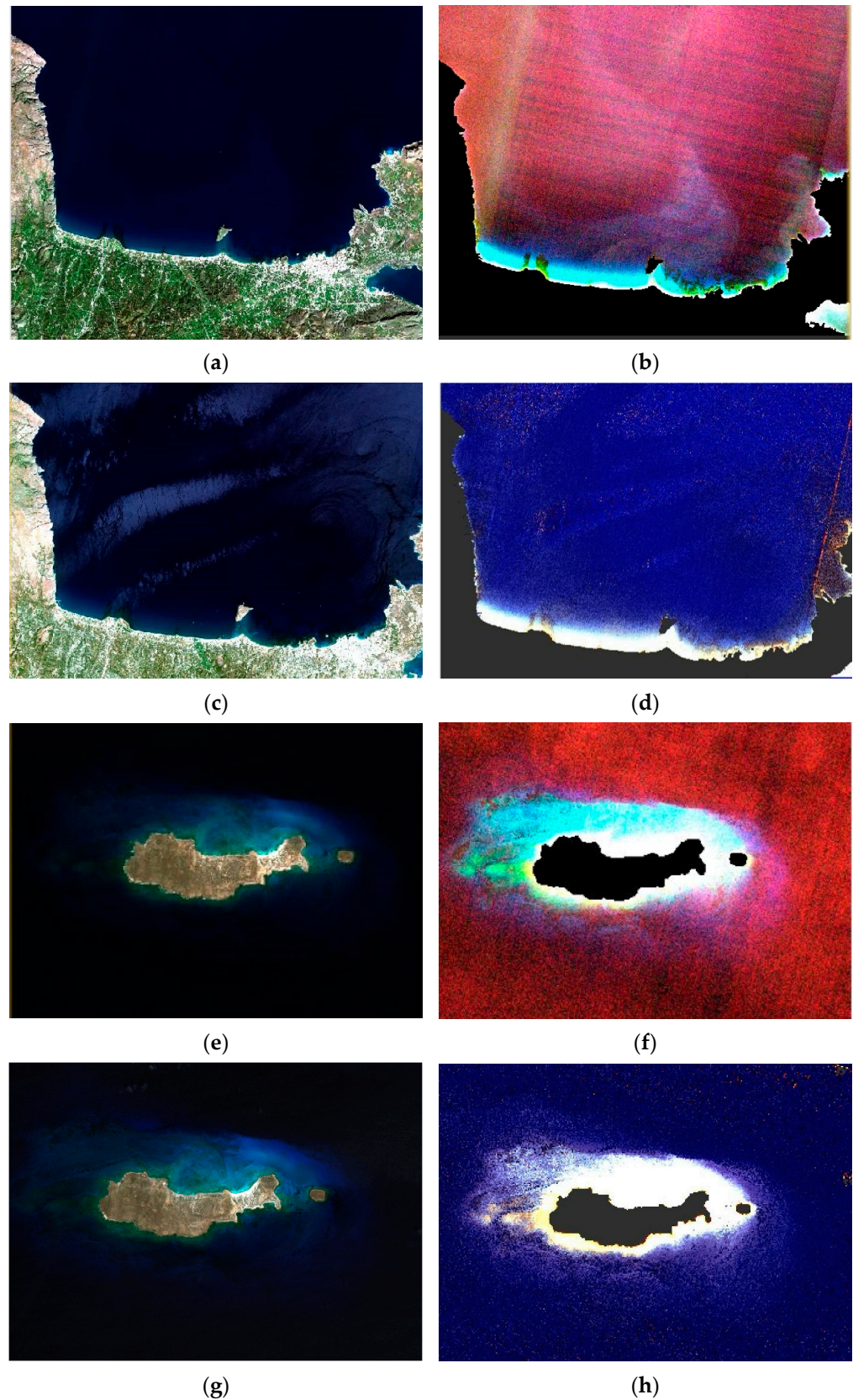


Figure 4. AC processor applied to summer and winter periods for both study areas. Chania Gulf: (a) winter 2022 imagery, (b) winter 2022 Acolite DSF imagery, (c) summer 2022 imagery, and (d) summer 2022 C2RCC imagery. Chrissi Island: (e) winter 2022 imagery, (f) winter 2022 Acolite DSF imagery, (g) summer 2022 imagery, and (h) summer 2022 C2RCC imagery.

4.2. Optical Water Properties Analysis

The diffuse attenuation, absorption, and backscattering coefficients describe the water's optical properties for both study areas. The breakdown of these coefficients shows a similar pattern for both study areas, as seen in Figure 5. Overall, the diffuse attenuation coefficient describes how rapidly light diminishes with depth. A higher value indicates that light diminishes faster, suggesting murkier waters, while a lower value suggests more transparent waters. Hence, the values show a general decrease for winter datasets as depth increases. This indicates that the water is more turbid in deeper parts due to light attenuation. The higher values near the shore or in shallower waters indicate greater particle concentration due to the influence of river run-off and sediment transport. Like in winter, the values decrease with depth during spring. This pattern suggests that the surface waters are relatively murkier, and clarity decreases with depth. The change from winter to spring might be less pronounced, but the general trend of more transparent waters at depth remains consistent. Afterward, the absorption represents the fraction of light absorbed by substances in the water, such as dissolved organic matter, phytoplankton, and detritus. A higher absorption coefficient suggests that more light is absorbed, decreasing water clarity, while a lower value suggests more transparent water. During winter, the absorption values of all bands generally decrease with depth; thus, this trend indicates that the amount of absorbing substances (like phytoplankton or dissolved organic matter) is higher near the surface and decreases in the deeper parts.

Similarly, the backscattering coefficient indicates the amount of incident light scattered back out of the water. A higher value implies more particles that scatter light, while a lower value means more transparent water. Concerning winter datasets, the backscattering coefficients decrease with depth, implying that there are fewer particles in deeper waters. This pattern is consistent with the trend observed for the absorption coefficient. During the spring, the backscattering coefficients also tend to decrease with depth. As for the summer season data, the process and outcome were conducted under C2RCC; the optical properties evaluated were the diffuse attenuation, total absorption, and backscattering coefficients.

The Interplay between these optical properties and bathymetry estimates was evident with the turbidity variation shown in formazin nephelometric units (FNU), measured using an infrared spectral band. The multiplot on the right illustrates the SPM fluctuations in g m^{-3} . The diffuse attenuation increases when there are more water scatterers in the water, and, therefore, more signal from the water and less signal overall from the bottom surface—i.e., a smaller fraction of the signal is derived from the reflectance of the bottom, so there are larger uncertainties.

By scattering light in various directions, high backscattering values can introduce noise into the satellite data, leading to potential discrepancies in the depth estimates [21]. One can see that the general pattern variation was stable and could be located up to approximately 10 m in depth. However, a chlorophyll concentration of 3.5 mg/m^3 was considered to indicate a low (not eutrophic) water body; hence, its impact on SDB estimates was assumed to be minimal and was neglected in the investigation process. Additionally, the summer variations in Chrissi Island dominated compared to the Chania Gulf, where chlorophyll is mainly sourced from shallow-water flora. Photosynthesis becomes more active as the days get longer and the weather gets warmer.



(a) (b)
Figure 5. Typical AOP and IOP variations on a seasonal basis in 2020 for: (a) the Chania Gulf and (b) Chrissi Island.

4.3. SDB Model

The linear method demonstrated outstanding performance in spring and summer, utilizing the green band, while the band ratio and IOPLM methods showed lower accuracy in the Chania Gulf results, as shown in Figure 6a. Processing in spring was carried out after C2RCC’s atmospheric correction, due to the poor performance of Acolite DSF, which produced dark pixels or zero radiance returns. However, Acolite DSF was used for atmospheric corrections in autumn. All methods were noted to underestimate the depth values in deeper areas.

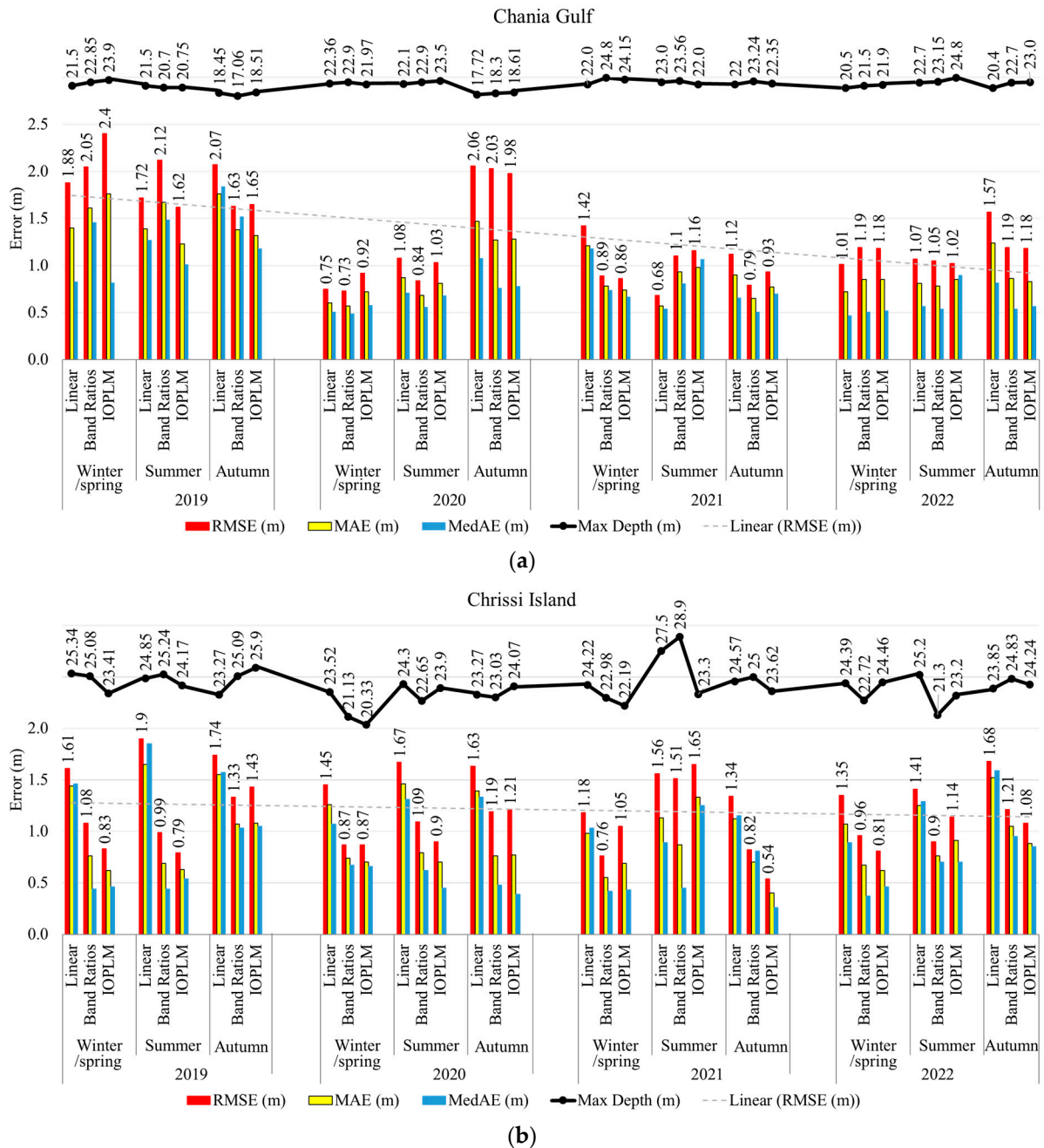


Figure 6. Error metrics of SDB estimates across all seasons for: (a) the Chania Gulf and (b) Chrissi Island.

In summer and autumn, the coastal blue-to-green band ratio was dominant, while spring favored green-blue and blue-green combinations. In 2020, all methods performed exceptionally well in winter and summer, but the accuracy declined significantly (by nearly 50%) in autumn, resulting in depth underestimations in deeper regions. Coastal blue-green

ratios dominated in winter and summer, whereas blue-green combinations were prevalent in autumn. By 2022, the linear method maintained superior performance in winter and summer, with winter calculations employing blue and green bands. The other methods performed consistently across all seasons, using coastal blue-green ratios in winter and autumn, and green-blue or blue-green ratios during summer.

For Chrissi Island, the linear method demonstrates consistent performance throughout the year, relying solely on the green band, with its winter predictions being the most accurate. In contrast, the band ratio and IOPLM methods perform well in spring and summer but degrade in autumn. In 2020, both methods yielded commendable results in winter and spring but underestimated depths beyond 20 m during spring and showed reduced efficacy in autumn, as shown in Figure 6b. The summer outputs from the C2RCC processor highlighted the influence of sunglint on the satellite imagery over Chrissi Island. Across all seasons, the linear method excelled in spring, while the IOPLM method performed best in autumn when combining blue, coastal blue, and green bands. However, the results were inconsistent across different years and seasons.

By 2022, the linear method maintained a stable performance, leveraging the green band, while the band ratio and IOPLM methods showed strong results throughout the year, with minor declines in autumn. The IOPLM method primarily used the coastal blue and green band combination, whereas the band ratio method employed blue-green ratios for winter and autumn and green-blue ratios for summer. A mild underestimation of depths was observed with the band ratio method in winter and summer, as shown in Figure 6b, with all methods estimating depths at around 24 m in autumn.

The results indicate that the band ratio and IOPLM methods performed effectively across all seasons, while the linear method delivered consistent but less accurate estimates. Furthermore, IOPLM predicted better depth estimates in almost the entire study period. Figure 6 represents the average RMSE metrics for every year and every method to provide a more comprehensive view of their performance. It is noticeable that the linear method delivered less accurate estimates but was consistent with the mean RMSE of 1.5 m. The other two methods were also stable over the study period, close to the mean RMSE of 1.0 m, showing slightly better results with the IOPLM method.

In this study, the MAPE was determined by utilizing the best results over each year among the three methods for both study sites. The core aim of this investigation was to evaluate the two water bodies' unique characteristics and the effectiveness of the SDB methods, under the premise that using the same passive satellite sensor with identical filtering options would yield imagery with consistent quality attributes. Figure 7 represents every method's calculated mean MAPE value for both study areas.

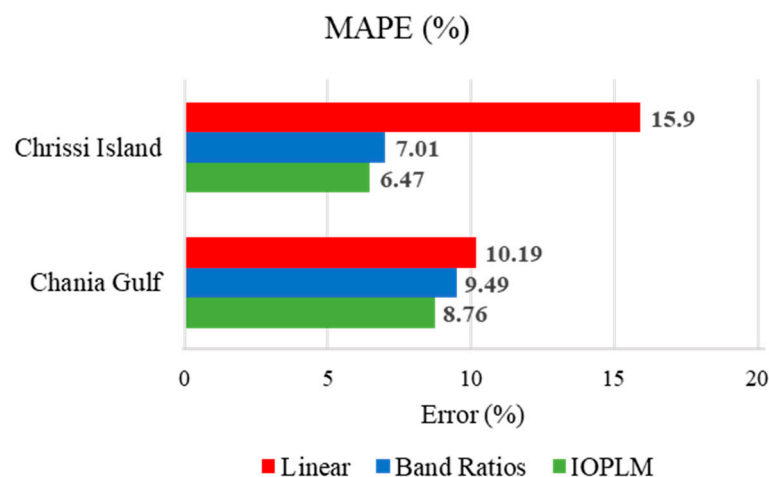


Figure 7. MAPE metric evaluation of SDB methods concerning both study sites.

Furthermore, the spatiotemporal variations in the SDB estimates of every tested method were structured in alignment with a season-centric approach. They were also divided into two parts: the Chania Gulf (Figure 8) and Chrissi Island (Figure 9). The data encompassed depth profile graphs across the three SDB methodologies, bathymetry maps, and an investigation of the geolocation accuracy of the satellite products.

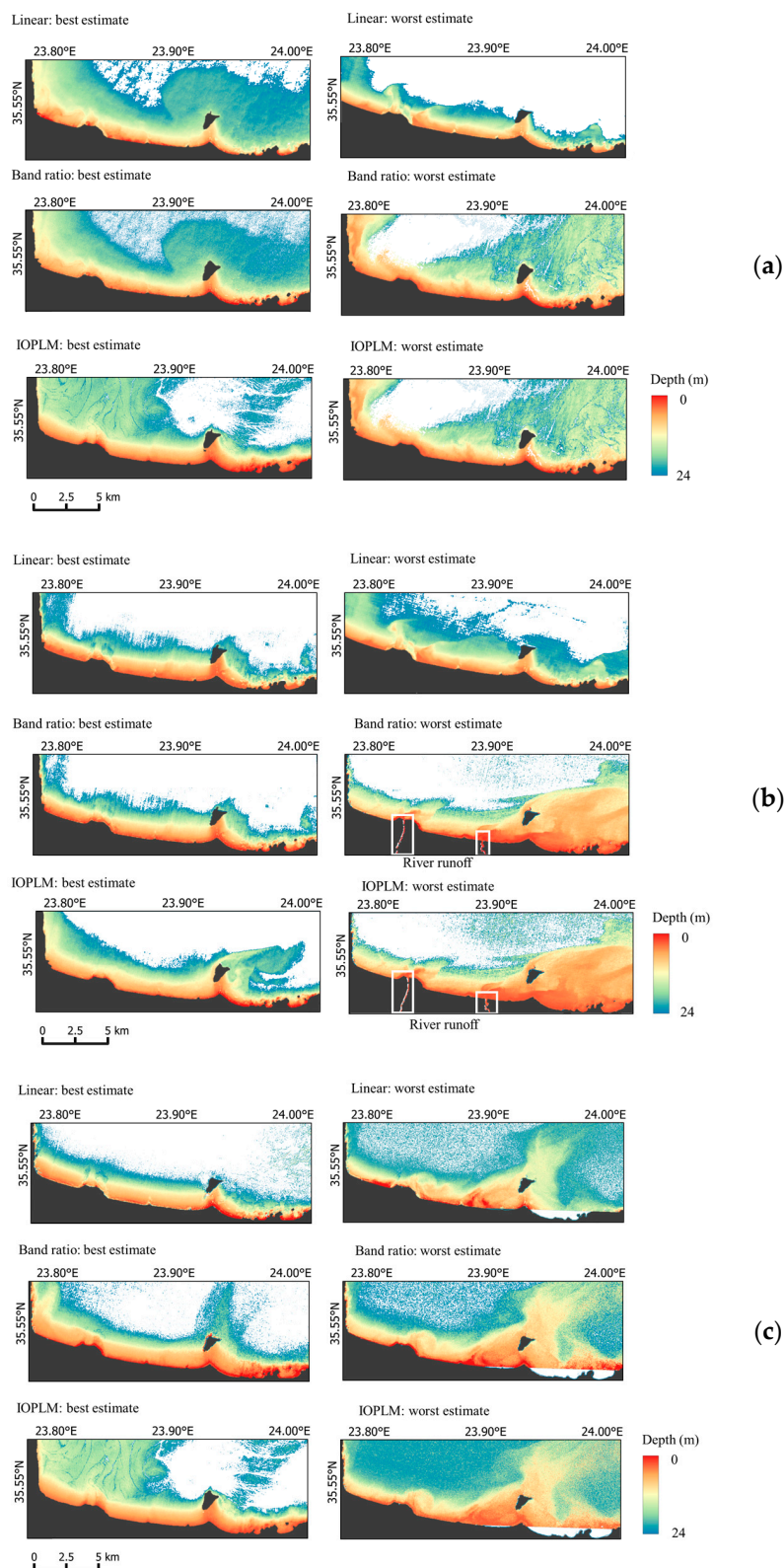


Figure 8. The results, compared using the typical SDB model for the Chania Gulf: (a) autumn, (b) winter/spring, and (c) summer.

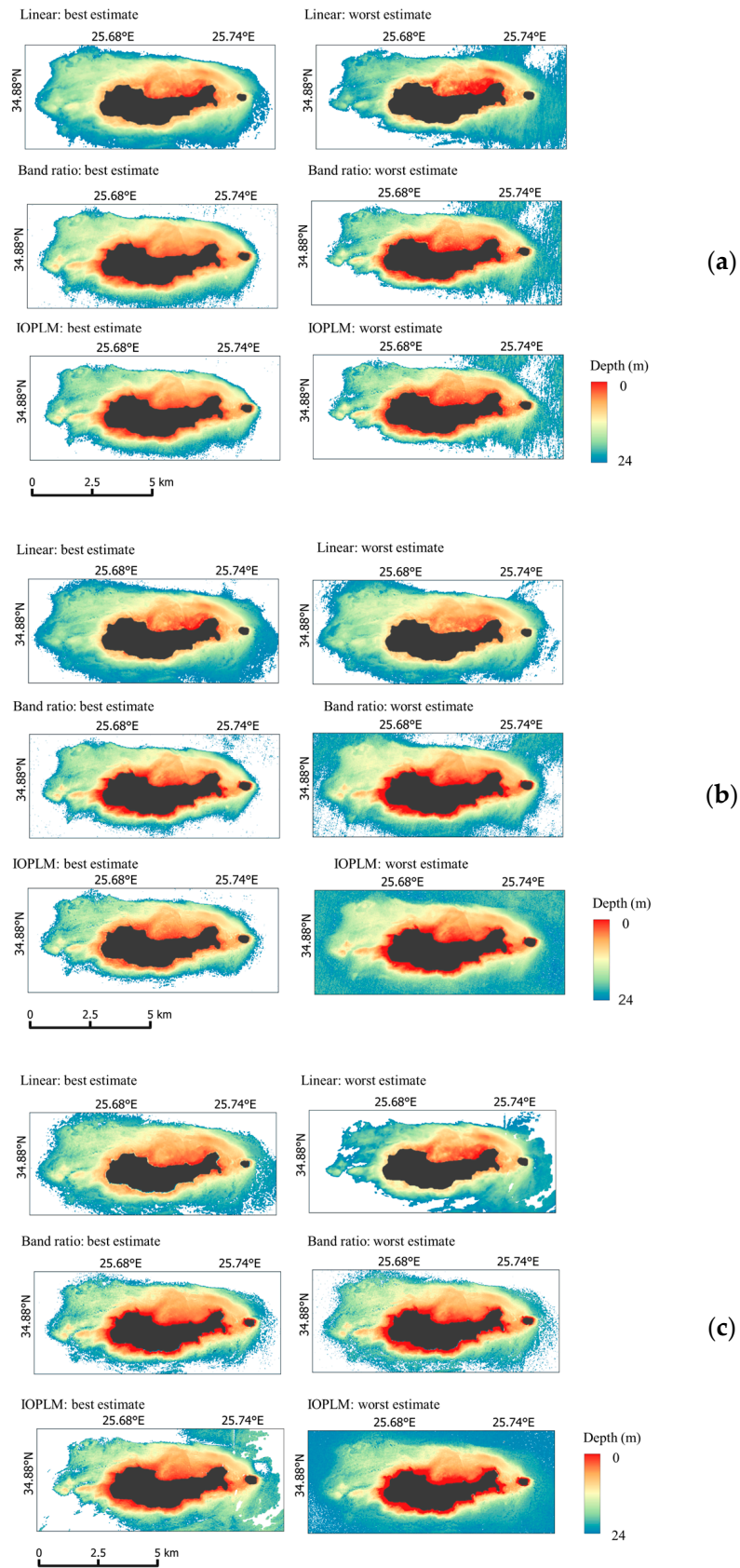


Figure 9. The results, compared using the typical SDB model for Chrissi Island: (a) autumn, (b) winter/spring, and (c) summer.

The variability in the optical milieu of Chania Gulf posed challenges for satellite-derived bathymetry in specific seasons, most notably when influenced by local river runoff. Despite these challenges, the general transparency of the water remained evident. The linear method displayed remarkable performance in the Chania Gulf compared to Chrissi Island. The band ratio transformation likewise showed exceptional and consistent capabilities for feature mapping across all seasons, albeit with minor fluctuations during instances with elevated turbidity. The IOPLM method was similarly proficient in capturing bathymetric variations in the Gulf, yielding dependable outcomes. Nonetheless, the method displayed heightened sensitivity to changes in IOPs during reduced water clarity, whether caused by river runoff or wind-induced shallow-water mixing.

The maximum depth estimations were slightly lower across all methods in deeper areas, particularly during late summer and autumn. The western part of the Gulf, which primarily comprises a sandy seabed, was mapped more accurately than the eastern half, which is dominated by rocky outcrops. This disparity could be due to the difference in bottom albedo, with sandy constituents reflecting more light than the darker, less reflective rocky areas. In addition, the gradual shift from shallow to deep waters in the Gulf contributed to better performance, particularly for the linear method. The maximum reliable depth estimation was less than that of Chrissi Island, at close to 21 m.

5. Discussions

The multispectral image's coastal blue or blue with green band combinations showed a closer relationship with depth changes and provided more accurate information. It can be seen that the linear method tends to overestimate depths, even during its optimal performance period. This was evident in the western, shallow part of the island, where the depth variations between 7 m and 10 m were not adequately derived or better than estimated. Similar behavior was recorded for the southern rocky seabed, where the linear method tends to produce a misinterpretation of depths. The other two methods that count the actual band responses described the bathymetry variations more effectively.

In the areas around Chrissi Island featuring steeper depth gradients, the precision of satellite-derived depth estimates showed a decline, as indicated in the bathymetry plot. This reduction in accuracy was particularly noticeable during summer and autumn, especially for depths exceeding 20 m. The impact was most significant in the linear method and band ratio transformation. Factors like shadowing effects and variations in water surface optical properties contributed to less accurate estimates. However, the IOPLM method, designed to account for any inherent optical properties directly, was more successful in mitigating these challenges.

Considering the SDB methods' performance, a possible key factor of the inaccurate overestimations made with midsummer–early autumn products was a temperature gradient between the near surface (0.5 m in depth) and the bottom (25.2 m in depth) of approximately 5.2 °C (differences obtained from the Copernicus Marine Service (CMEMS)) [41]. The influence of the temperature gradient, as shown in Ref. [42], indicates that when the temperature gradient exceeds 4 °C, the resulting image exhibits greater divergence from the original image at the initial temperature. Hence, the distortion caused by the temperature gradient could affect the light path and the backscattering strength and geometry. Additionally, the IOP and bathymetry estimates correlate with each other, as diffuse attenuation increases; for example, in shallow waters, satellite-derived depth estimates tend to be less accurate. The multispectral image's coastal blue or blue with green band combinations showed a closer relationship to depth changes and provided more accurate information. Figure 10 illustrates a set of samples gathered in the island's northern part (summer 2020), in waters ranging from very shallow to deep, to investigate the remote sensing response

with depth changes. The remote sensing reflectance (R_{rs}) value showed a peak response in the green band (560 nm) regarding very shallow waters, followed by the blue band (490 nm) and the coastal blue (443 nm) band with lower values. In contrast, in shallow and intermediate waters, the transition between the band's response was smooth, with the blue band (490 nm) maintaining the highest values, closely followed by bands of green (560 nm) and lower coastal blue (443 nm). As the depth increased, the responses of the coastal blue and blue bands converged, while the green band's response was consistently lower, and, in deep areas over 21 m, the response of coastal blue dominates against the others; however, this behavior seemed erroneous.

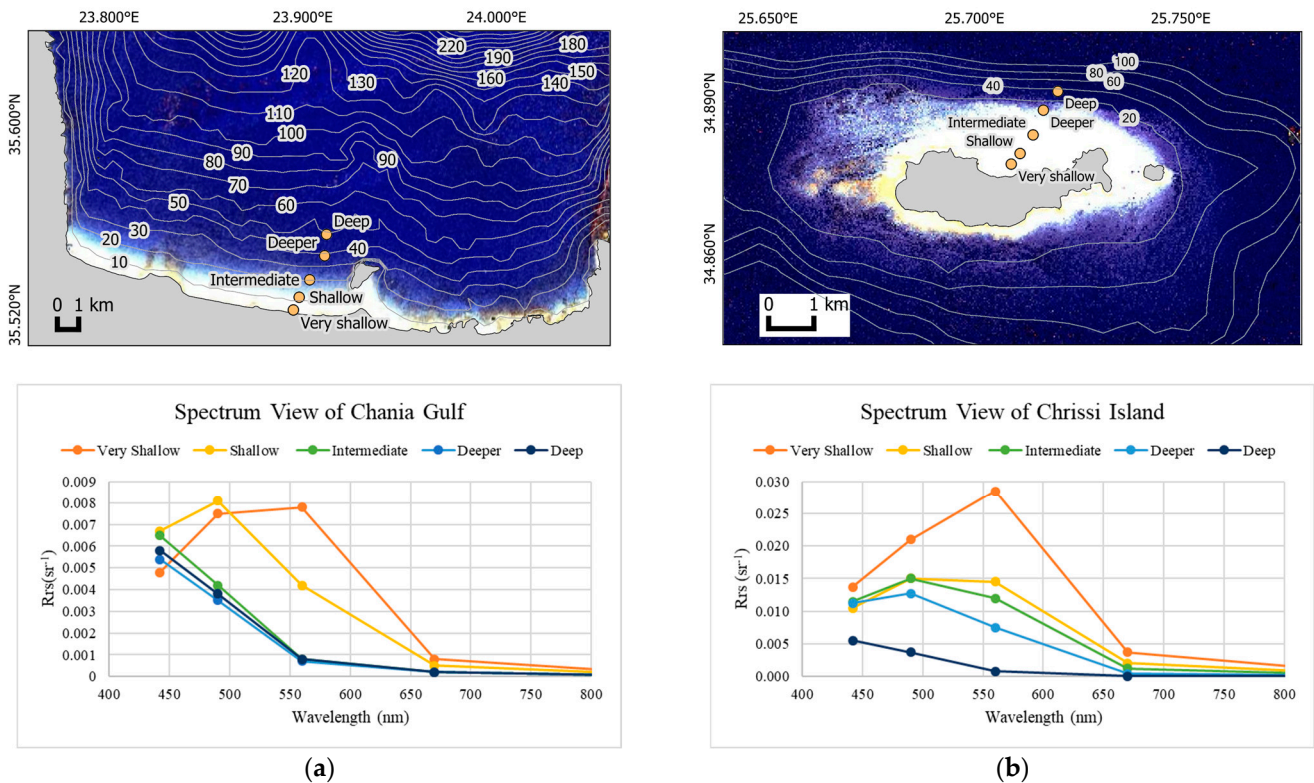


Figure 10. Spectrum analysis concerning remote sensing reflectance (R_{rs}) for (a) the Chania Gulf and (b) Chrissi Island, with the spatial distribution of sample points depicted in the top figures. The figures also include location and depth information derived from the contour lines (measured in meters).

5.1. Assessment of Model Accuracy

The most favorable result was obtained using the IOPLM method during autumn 2021, as illustrated in Figure 11. An RMSE value of 0.54 m was achieved compared to the field measurements, which serve as the reference standard. Additionally, boundaries for CATZOC B, adjusted to a depth of 24 m under IHO's guidelines, were incorporated into the plot to validate the bathymetric estimates. The total number of individual depth estimates laid within these boundaries was 20 out of 21 (95.24%), delineating the high accuracy of the SDB outcome, even at depths of 24 m.

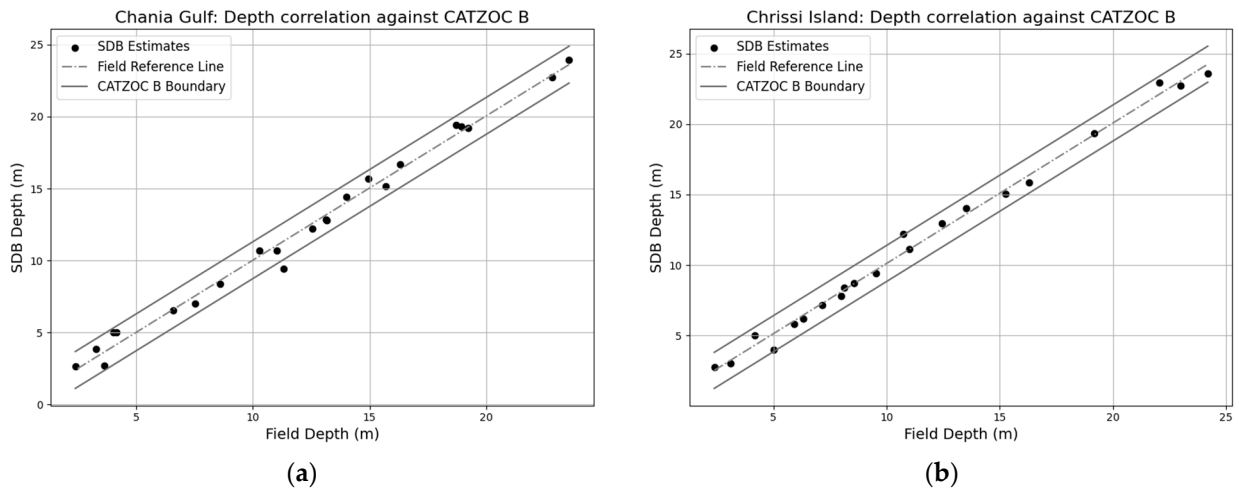


Figure 11. Error classification of the SDB model based on CATZOC: (a) the Chania Gulf and (b) Chrissi Island.

In assessing bathymetry mapping methods for Chrissi Island, the linear technique underperformed compared to ratio-based methods, as seen in Figure 12. It overestimated depths in the western shallow and southern rocky areas, with RMSE values ranging from 1.18 m to 1.90 m. In contrast, the band ratio and IOPLM methods achieved superior results, with the best RMSE values of 0.76 m and 0.54 m, and worst values of 1.68 m and 1.65 m, respectively. The linear method’s overestimation was likely due to rocky outcrops absorbing more light, affecting the depth readings, particularly in the northeastern region (6 to 12 m in depth). The band ratio and IOPLM methods proved more robust, with IOPLM being the most suitable for the area, especially when using high-quality Sentinel-2 MSI imagery during winter and spring, which was processed with the Acolite DSF atmospheric correction algorithm.

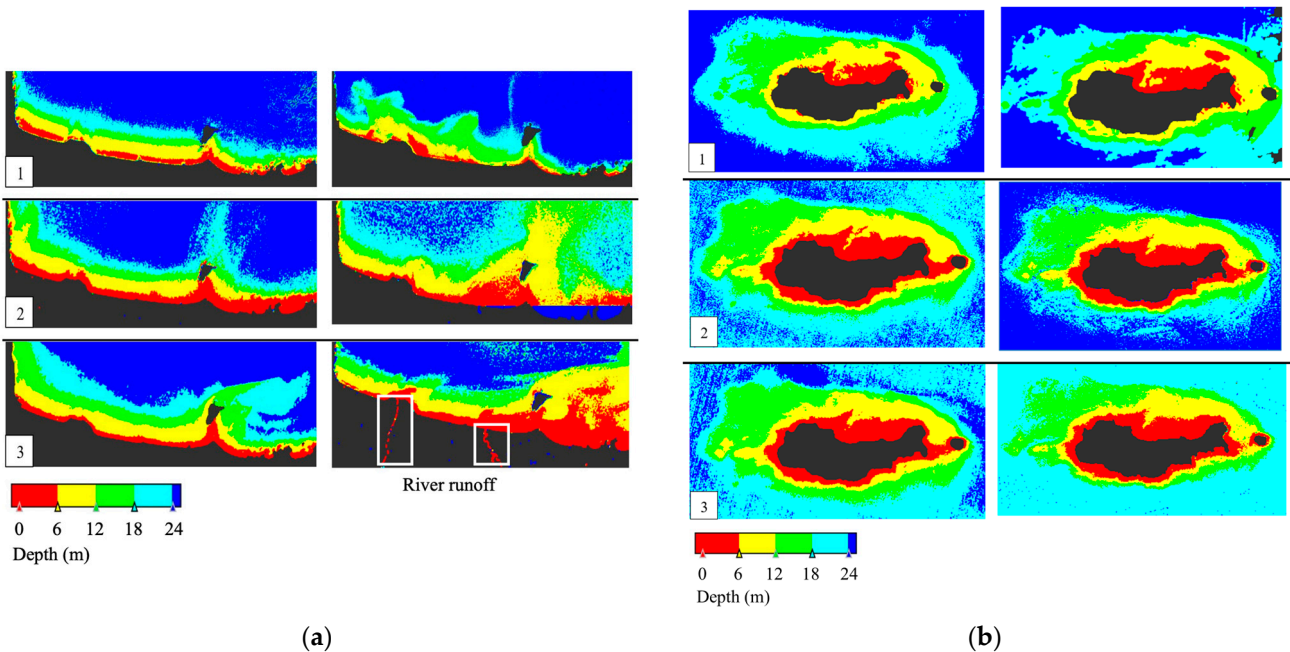


Figure 12. Multi-bathymetric plot for (a) Chania Gulf and (b) Chrissi Island: the first row (1) shows the linear method’s best performance on the left and its worst on the right. The second row (2) presents the band ratio method’s best performance on the left and its worst on the right. The third row (3) displays the IOPLM method’s best performance on the left and its worst on the right.

In the Chania Gulf, performance varied significantly among the methods, mainly due to late spring turbidity changes from local river runoff as seen in Figure 12a. The IOPLM method was particularly sensitive to these variations. The linear method excelled in summer 2021, with an RMSE of 0.68 m, but struggled in autumn 2019, recording an RMSE of 2.07 m, indicating major overestimation. The band ratio technique also performed well, achieving an RMSE of 0.64 m in summer 2018, but its performance declined in summer 2019 (2.12 m RMSE), primarily underestimating depths in the eastern area. IOPLM's best performance was in spring 2021 (0.86 m RMSE), while its least effective result was in spring 2019 (2.40 m RMSE), when it showed significant underestimation, particularly in the eastern Gulf.

The linear method's poor performance was attributed to its reliance on a single spectral band, limiting its adaptability to changing water properties. In contrast, the ratio-based methods, particularly IOPLM, were sensitive to variations, notably in 2019, capturing depth estimations that were influenced by river inflows. Given the geographic conditions and the quality of Sentinel-2 MSI imagery, the band ratio technique emerged as the most versatile method, especially in late summer or early autumn. While the Acolite DSF algorithm was effective, the C2RCC processor also performed well in summer, particularly under severe sunglint conditions, delivering notable results for SDB estimates.

5.2. Kalman Filter (KF)

Data assimilation methods, such as Kalman filtering, effectively extract information from noisy observations. When combined with a physics-based model, this approach provides accurate bathymetry estimates and an uncertainty assessment [43]. Applying the Kalman filter significantly reduces estimation errors and results in smoother data outputs. Figure 13 illustrates the results after applying the filter to the Chrissi Island study area using the linear and IOPLM methods. The filter was applied to the linear SDB estimates, which showed a more significant depth discrepancy to the field data, and the IOPLM method, which provided more precise depth estimates. The Kalman filter smoothed the best SDB estimates and improved accuracy at greater distances. However, for linear estimates, only 51% of the data samples fell within the TVU range of the IHO special order, in contrast with the IOPLM data, wherein 100% of samples fell within the TVU range.

The performance of the SDB estimation methods showed significant improvement after applying an update, as indicated in Table 2. Initially, the linear method exhibited high error rates due to using lower-quality sample data, with an RMSE of 1.81, MAE of 1.48, and MedAE of 1.16. After the update, these errors were substantially reduced: the RMSE decreased to 0.47, MAE to 0.37, and MedAE to 0.30, reflecting a marked enhancement in accuracy. In contrast, the IOPLM method started with much lower error rates—an RMSE of 0.54, MAE of 0.40, and MedAE of 0.27—and the update further enhanced its performance, reducing the RMSE to 0.05, MAE to 0.04, and MedAE to 0.02.

Additionally, applying the KF across all seasonal periods demonstrated a consistent improvement in RMSE for both study areas, as seen in Figure 14, with an average reduction of approximately 50 cm and a decrease in uncertainty by about 30%. An exception was observed in the 2019 dataset for the Chania Gulf, where the initial estimates showed the largest positional discrepancies. Notably, the process noise was modeled to allow the prediction covariance to increase proportionally with depth, with an average increment of around 20 cm. When merging all seasonal SDB estimates to generate an average depth estimate across periods, the Chania Gulf achieved the best RMSE improvements. The initial RMSE of 55 cm was reduced to 14 cm after updating, while the updated uncertainty decreased to 47 cm from the initial 105 cm. A similar trend is observed in Chrissi Island,

where the initial RMSE of 63 cm improved to 18 cm after updating, and the uncertainty dropped from 102 cm to 51 cm.

It is important to note that the filter was applied exclusively to SDB estimates that corresponded directly to the field measurement data (i.e., those with matching spatial coordinates and depth information). Further investigation is necessary when working with the entire area generated by SDB and time series data, especially concerning error prediction and when modeling and refining the SDB algorithms. Nevertheless, the method’s ability to dynamically adapt is evident.

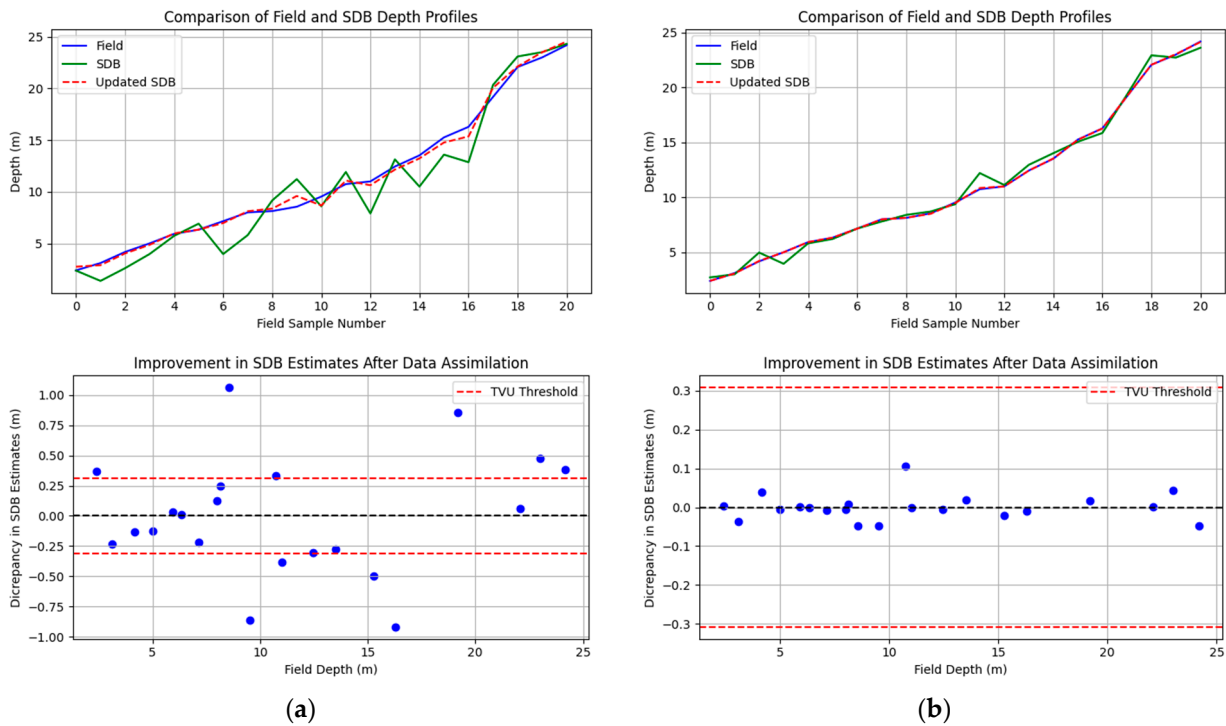


Figure 13. SDB estimations before and after KF employment for Chrissi Island data: (a) linear SDB estimates and (b) IOPLM SDB estimates.

Table 2. Metrics response of the linear method before and after KF improvement.

SDB Method	Metric	Value (m)
Linear	RMSE	1.81
	RMSE updated	0.47
	MAE	1.48
	MAE updated	0.37
	MedAE	1.16
	MedAE updated	0.30
IOPLM	RMSE	0.54
	RMSE updated	0.05
	MAE	0.40
	MAE updated	0.04
	MedAE	0.27
	MedAE updated	0.02

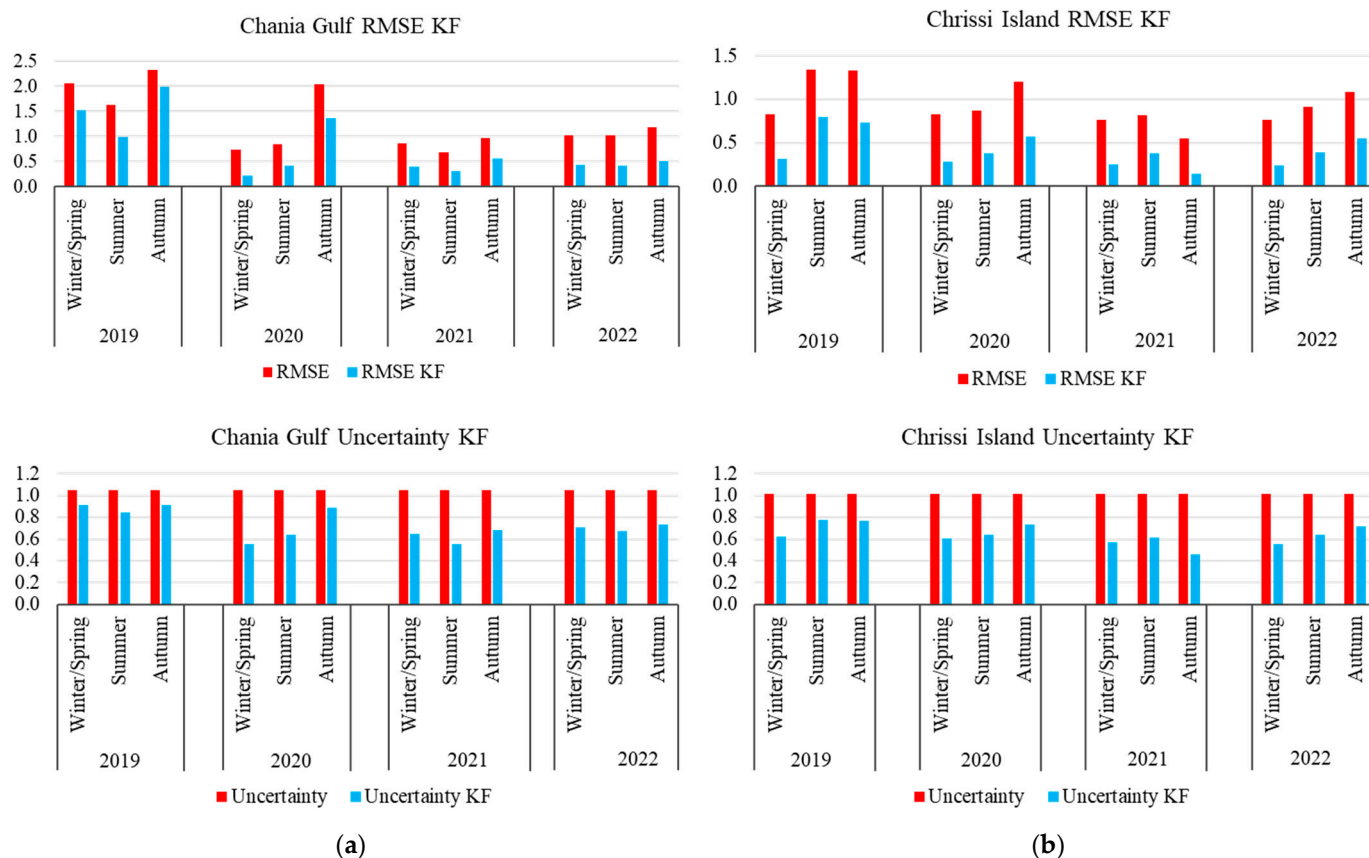


Figure 14. Example of KF implementation applied to the initial SDB estimates in the seasonal period, demonstrating the improvement in RMSE and uncertainty after assimilating field measurements: (a) the Chania Gulf and (b) Chrissi Island.

6. Conclusions

This research extensively explored the complexities and nuances of satellite-derived bathymetry (SDB) in the Eastern Mediterranean. This study’s multifaceted approach, which considers the region’s unique hydrodynamic characteristics, spatiotemporal variations, and variations in optical properties, significantly contributes to the knowledge in this specific field. This study underscored the critical role that spatiotemporal variations play in the accuracy of SDB estimates. The significance of these variations cannot be overstated; they serve as a foundation for developing new methodologies and refining the existing ones to improve data reliability in hydro-spatial applications.

One of the most significant findings of this research was the strong correlation between water surface optical properties and SDB estimates. Explicitly identifying this correlation could enable researchers and practitioners to develop more accurate models for bathymetric estimation. Moreover, the need for concurrent data on optical properties and bathymetry has been substantiated, offering a more holistic approach to underwater mapping and analysis. The in-depth comparative analysis of various SDB methods provides actionable insights into their performance under different conditions over approximately five years. This study has identified specific methods that offer higher reliability in correlation with the optical properties of water in the Eastern Mediterranean. This is critical for decision-makers who must choose the most appropriate method for their specific needs, thereby enhancing the quality and reliability of hydro-spatial data.

By combining different SDB methods into merged products, this study achieved unprecedented accuracy and reliability in its bathymetric estimates. This multi-method approach represents a significant advancement in the field, suggesting a new standard

for future research and applications. It shows that the robustness and reliability of these merged products offer tangible benefits for applications that require a high degree of precision, such as navigation safety and marine conservation efforts. The study's findings on the influence of seasonal and weather patterns on SDB estimates provide valuable insights for future research and applications. These findings have practical implications, as they assist researchers and practitioners in planning data collection schedules to avoid times when turbidity or other factors may affect data accuracy. Thus, understanding these patterns can lead to more strategic data collection and better outcomes.

While the primary focus of the research was to investigate known variables, unexpected findings also emerged. These anomalies in SDB method performance under unique conditions offer opportunities for further investigation. Unpacking these unexpected findings could pave the way for new research directions, leading to a deeper understanding of SDB methodologies and their limitations. While all three methods offer valuable insights into Chrissi Island's bathymetry models, their performance varies with the seasons and the corresponding optical property fluctuations. The IOPLM method, given its sophisticated approach, consistently emerges as the most reliable method across both regions. Understanding the interplay between these methods, optical properties, and depth profiles is crucial for informed marine and coastal management decision-making. Correlating the variations in optical properties with the method statistics reveals that seasons with higher turbidity or significant suspended matter can hinder the accuracy of satellite-derived bathymetry, especially with the linear method. Such particles scatter light differently, affecting the satellite's ability to discern depth based on reflectance alone.

7. Future Research

While SDB technology has advanced markedly, challenges still exist around fluid dynamics, ocean color, and clarity, which impact SDB estimation. Consequently, over the past two years, many researchers have investigated the feasibility of deriving bathymetric information from coastal regions solely through satellite-based spatial data [1,2,9,29,31,44,45]. Launched in September 2018, the Ice, Cloud, and Elevation Satellite-2 (ICESat-2) features the advanced topographic laser altimeter system (ATLAS), a photon-counting LiDAR system operating at a wavelength of 532 nm. Initial data from ICESat-2 have underscored its capability to provide global bathymetric LiDAR measurements in shallow coastal waters with depths of less than 40 m, which can be fused with multispectral imagery to generate SDB estimates. Furthermore, advancements in machine learning (ML) algorithms and artificial intelligence (AI) could potentially automate processing further and reduce the limitations imposed by user–software interaction and data volume [2,9,46].

In summary, satellite-derived bathymetry has made tremendous advances, enabled by improved sensors and algorithms. While challenges remain, continued technological improvements indicate its increasing role in coastal mapping applications as a supplemental survey method, offering cost-effective seabed data for regions not yet covered by conventional acoustic or LiDAR sensors and generating more accurate data, given the right environmental conditions. Its cost-efficiency, spatial coverage, and timeliness make it a strong choice for various hydro-spatial tasks. These include scouting remote areas, mapping extremely shallow zones that pose navigational risks, and routinely tracking changes in shallow sea floors [44].

Author Contributions: Conceptualization, F.M. and H.S.; methodology, I.T.; software, I.T. and F.M.; validation, F.M. and I.T.; formal analysis, I.T. and F.M.; investigation, F.M. and I.T.; resources, I.T.; data curation, I.T.; writing—original draft preparation, F.M. and I.T.; writing—review and editing, F.M.; visualization, F.M. and I.T.; supervision, H.S. All authors have read and agreed to the published version of the manuscript.

Funding: This research is supported by internal funding from HafenCity University (HCU).

Data Availability Statement: The satellite imagery data are openly accessible via the ESA portal. The terrestrial data for training and model validation can be requested via email to the corresponding author.

Acknowledgments: The authors would like to thank the ESA for providing free open-access satellite imagery. In addition, the authors would like to thank the Greek Navy for providing the field data.

Conflicts of Interest: The authors declare no conflicts of interest.

References

1. Ashphaq, M.; Srivastava, P.K.; Mitra, D. Review of Near-Shore Satellite Derived Bathymetry: Classification and Account of Five Decades of Coastal Bathymetry Research. *J. Ocean Eng. Sci.* **2021**, *6*, 340–359. [CrossRef]
2. Louvart, P.; Cook, H.; Smithers, C.; Laporte, J. A New Approach to Satellite-Derived Bathymetry: An Exercise in Seabed 2030 Coastal Surveys. *Remote Sens.* **2022**, *14*, 4484. [CrossRef]
3. Stumpf, R.P.; Holderied, K.; Spring, S.; Sinclair, M. Determination of Water Depth with High-Resolution Satellite Imagery over Variable Bottom Types. *Limnol. Oceanogr.* **2003**, *48*, 547–556. [CrossRef]
4. Lyzenga, D. Passive Remote-Sensing Techniques for Mapping Water Depth and Bottom Features. *Appl. Opt.* **1978**, *17*, 379–383. [CrossRef]
5. Jupp, D. International Journal of Remote Reconstruction of Sand Wave Bathymetry Using Both Satellite Imagery and Multi-Beam Bathymetric Data: A Case Study of the Taiwan Banks. In Proceedings of the Symposium on Remote Sensing of the Coastal Zone, Gold Coast, QLD, Australia, 7–9 September 1988.
6. Lee, Z.; Carder, K.L.; Arnone, R.A. Deriving Inherent Optical Properties from Water Color: A Multiband Quasi-Analytical Algorithm for Optically Deep Waters. *Appl. Opt.* **2002**, *41*, 5755. [CrossRef]
7. Zhang, X.; Ma, Y.; Zhang, J. Shallow Water Bathymetry Based on Inherent Optical Properties Using High Spatial Resolution Multispectral Imagery. *Remote Sens.* **2020**, *12*, 3027. [CrossRef]
8. Streftaris, N.; Zenetos, A.; Papatthanassiou, E. Globalisation in Marine Ecosystems: The Story of Non-Indigenous Marine Species across European Seas. *Oceanogr. Mar. Biol.* **2005**, *43*, 419–453. [CrossRef]
9. Mandlburger, G. A Review of Active and Passive Optical Methods in Hydrography. *Int. Hydrogr. Rev.* **2022**, *28*, 8–52. [CrossRef]
10. Chaikalis, S.; Parinos, C.; Möbius, J.; Gogou, A.; Velaoras, D.; Hainbucher, D.; Sofianos, S.; Tanhua, T.; Cardin, V.; Proestakis, E.; et al. Optical Properties and Biochemical Indices of Marine Particles in the Open Mediterranean Sea: The R/V Maria S. Merian Cruise, March 2018. *Front. Earth Sci.* **2021**, *9*, 614703. [CrossRef]
11. Drakopoulou, P.; Kapsimalis, V.; Parcharidis, I.; Pavlopoulos, K. Retrieval of Nearshore Bathymetry in the Gulf of Chania, NW Crete, Greece, from WorldView-2 Multispectral Imagery. *Proc. SPIE* **2018**, *54*, 10773. [CrossRef]
12. Natura 2000 Natura 2000—Standard Data Form: Site GR4340003. Available online: <https://natura2000.eea.europa.eu/Natura2000/SDF.aspx?site=GR4340003> (accessed on 3 September 2023).
13. ESA S2 MSI ESL Team. Copernicus Space Component Sentinel Optical Imaging Mission Performance Cluster Service Sentinel-2 Annual Performance Report-Year 2022. 2023. Available online: <https://sentinel.esa.int/documents/247904/4868341/OMPC.CS.DQR.001.12-2022+-+i83r0+-+MSI+L1C+DQR+January+2023.pdf> (accessed on 28 July 2023).
14. Mobley, C.D. *The Oceanic Optics Book*; IOCCG: Dartmouth, NS, Canada, 2022; 924p. [CrossRef]
15. Lyzenga, D. Shallow-Water Bathymetry Using Combined Lidar and Passive Multispectral Scanner Data. *Int. J. Remote Sens.* **1985**, *6*, 115–125. [CrossRef]
16. Chybicki, A. Mapping South Baltic Near-Shore Bathymetry Using Sentinel-2 Observations. *Polish Marit. Res.* **2017**, *24*, 15–25. [CrossRef]
17. Kutser, T.; Hedley, J.; Giardino, C.; Roelfsema, C.; Brando, V.E. Remote Sensing of Shallow Waters—A 50 Year Retrospective and Future Directions. *Remote Sens. Environ.* **2020**, *240*, 111619. [CrossRef]
18. Goodman, J.A.; Lee, Z.P.; Ustin, S.L. Influence of Atmospheric and Sea-Surface Corrections on Retrieval of Bottom Depth and Reflectance Using a Semi-Analytical Model: A Case Study in Kaneohe Bay, Hawaii. *Appl. Opt.* **2008**, *47*, F1–F11. [CrossRef] [PubMed]
19. Lee, Z.; Hu, C.; Shang, S.; Du, K.; Lewis, M.; Arnone, R.; Brewin, R. Penetration of UV-Visible Solar Radiation in the Global Oceans: Insights from Ocean Color Remote Sensing. *J. Geophys. Res. Ocean.* **2013**, *118*, 4241–4255. [CrossRef]
20. Philpot, W.D. Bathymetric Mapping with Passive Multispectral Imagery. *Appl. Opt.* **1989**, *28*, 1569. [CrossRef]
21. IOCCG. *Remote Sensing of Inherent Optical Properties: Fundamentals, Tests of Algorithms, and Applications*; IOCCG: Dartmouth, NS, Canada, 2006; Volume 5, ISBN 9781896246567.
22. Vanhellemont, Q. Adaptation of the Dark Spectrum Fitting Atmospheric Correction for Aquatic Applications of the Landsat and Sentinel-2 Archives. *Remote Sens. Environ.* **2019**, *225*, 175–192. [CrossRef]

23. Vanhellemont, Q. Sensitivity Analysis of the Dark Spectrum Fitting Atmospheric Correction for Metre- and Decametre-Scale Satellite Imagery Using Autonomous Hyperspectral Radiometry. *Opt. Express* **2020**, *28*, 29948. [[CrossRef](#)]
24. Caballero, I.; Stumpf, R.P. Atmospheric Correction for Satellite-Derived Bathymetry in the Caribbean Waters: From a Single Image to Multi-Temporal Approaches Using Sentinel-2A/B. *Opt. Express* **2020**, *28*, 11742. [[CrossRef](#)]
25. Brockman, C.; Doerffer, R.; Peters, M.; Stelzer, K.; Embacher, S.; Ruescas, A. Evolution of the C2RCC Neural Network for Sentinel 2 and 3 for the Retrieval of Ocean Colour Products in Normal and Extreme Optically Complex Waters. *Living Planet Symp.* **2004**, *740*, 54.
26. Ribeiro, M.I. *Kalman and Extended Kalman Filters: Concept, Derivation and Properties*; Institute for Systems and Robotics: Lisboa, Portugal, 2004; p. 42.
27. Mobley, C.D.; Stramski, D.; Paul Bissett, W.; Boss, E. Optical Modeling of Ocean Waters: Is the Case 1–Case 2 Classification Still Useful? *Oceanography* **2004**, *17*, 60–67. [[CrossRef](#)]
28. Mavraeidopoulos, A.K. Satellite Derived Bathymetry with No Use of Field Data. In Proceedings of the 2nd International Conference on Design and Management of Port, Coastal and Offshore Works, Thessaloniki, Greece, 24–27 May 2013; pp. 1–8.
29. Mavraeidopoulos, A.K.; Oikonomou, E.; Palikaris, A.; Poulos, S. A Hybrid Bio-Optical Transformation for Satellite Bathymetry Modeling Using Sentinel-2 Imagery. *Remote Sens.* **2019**, *11*, 2746. [[CrossRef](#)]
30. Chavez, P.S. An Improved Dark-Object Subtraction Technique for Atmospheric Scattering Correction of Multispectral Data. *Remote Sens. Environ.* **1988**, *24*, 459–479. [[CrossRef](#)]
31. Traganos, D.; Poursanidis, D.; Aggarwal, B.; Chrysoulakis, N.; Reinartz, P. Estimating Satellite-Derived Bathymetry (SDB) with the Google Earth Engine and Sentinel-2. *Remote Sens.* **2018**, *10*, 859. [[CrossRef](#)]
32. RBINS. *ACOLITE User Manual (QV—2 August 2021)*; Royal Belgian Institute of Natural Sciences (RBINS): Brussels, Belgium, 2021.
33. Hollingsworth, A.; Engelen, R.J.; Textor, C.; Benedetti, A.; Boucher, O.; Chevallier, F.; Dethof, A.; Elbern, H.; Eskes, H.; Flemming, J.; et al. Toward a Monitoring and Forecasting System for Atmospheric Composition: The GEMS Project. *Bull. Am. Meteorol. Soc.* **2008**, *89*, 1147–1164. [[CrossRef](#)]
34. Doerffer, R.; Schiller, H. The MERIS Case 2 Water Algorithm. *Int. J. Remote Sens.* **2007**, *28*, 517–535. [[CrossRef](#)]
35. Nechad, B.; Ruddick, K.G.; Neukermans, G. Calibration and Validation of a Generic Multisensor Algorithm for Mapping of Turbidity in Coastal Waters. In *Remote Sensing of the Ocean, Sea Ice, and Large Water Regions*; SPIE: Bellingham, WA, USA, 2009; Volume 7473. [[CrossRef](#)]
36. Nechad, B.; Ruddick, K.G.; Park, Y. Calibration and Validation of a Generic Multisensor Algorithm for Mapping of Total Suspended Matter in Turbid Waters. *Remote Sens. Environ.* **2010**, *114*, 854–866. [[CrossRef](#)]
37. Chai, T.; Draxler, R.R. Root Mean Square Error (RMSE) or Mean Absolute Error (MAE)? -Arguments against Avoiding RMSE in the Literature. *Geosci. Model Dev.* **2014**, *7*, 1247–1250. [[CrossRef](#)]
38. Willmott, C.J.; Matsuura, K. Advantages of the Mean Absolute Error (MAE) over the Root Mean Square Error (RMSE) in Assessing Average Model Performance. *Clim. Res.* **2005**, *30*, 79–82. [[CrossRef](#)]
39. Makridakis, S. Accuracy Measures: Theoretical and Practical Concerns. *Int. J. Forecast.* **1993**, *9*, 527–529. [[CrossRef](#)]
40. IHO. *S-44 6th Edition: IHO Standards For Hydrographic Surveys*; IHO: Monaco-Ville, Monaco, 2020.
41. Copernicus Marine Service (CMEMS). Sea Water Potential Temperature. Available online: <https://marine.copernicus.eu/access-data> (accessed on 27 August 2023).
42. Yin, M.Q.; Wang, L.; Zhao, S.M. Experimental Demonstration of Influence of Underwater Turbulence on Ghost Imaging. *Chin. Phys. B* **2019**, *28*, 1–6. [[CrossRef](#)]
43. Ghorbanidehno, H.; Lee, J.; Farthing, M.; Hesser, T.; Kitanidis, P.K.; Darve, E.F. Novel Data Assimilation Algorithm for Nearshore Bathymetry. *J. Atmos. Ocean. Technol.* **2019**, *36*, 699–715. [[CrossRef](#)]
44. Herrmann, J.; Magruder, L.A.; Markel, J.; Parrish, C.E. Assessing the Ability to Quantify Bathymetric Change over Time Using Solely Satellite-Based Measurements. *Remote Sens.* **2022**, *14*, 1232. [[CrossRef](#)]
45. Miller, R.L.; Del Castillo, C.E.; Mckee, B.A. *Remote Sensing of Coastal Aquatic Environments*; Springer: New York, NY, USA, 2005; ISBN 9781402030994.
46. Mohamed, H.; Nadaoka, K.; Nakamura, T. Towards Benthic Habitat 3D Mapping Using Machine Learning Algorithms and Structures from Motion Photogrammetry. *Remote Sens.* **2020**, *12*, 127. [[CrossRef](#)]

Disclaimer/Publisher’s Note: The statements, opinions and data contained in all publications are solely those of the individual author(s) and contributor(s) and not of MDPI and/or the editor(s). MDPI and/or the editor(s) disclaim responsibility for any injury to people or property resulting from any ideas, methods, instructions or products referred to in the content.